Synthetic Photoconductive Antenna Array for Terahertz 3D Imaging and Spectroscopy

M. Ait Assou, Georges Humbert, Aurelian Crunteanu, C. Decroze

Synthetic Photoconductive Antenna Array for Terahertz 3D Imaging and Spectroscopy

M. Ait Assou, G. Humbert, A. Crunteanu (*Member, IEEE)*, C. Decroze

***Abstract*— We propose a 3D imaging and spectroscopy approach in the terahertz (THz) domain based on the synthetic aperture (SA) imaging technique achieved using a time domain spectroscopy system (TDS). The proposed system enables the imaging and spectroscopy of an object in a stationary position in transmission configuration. We demonstrate the reconstruction of 3D amplitude images with a sub-millimeter resolution of a multi-material object from 0.6 to 1 THz using the back-projection algorithm. The reconstructed data is further used to characterize the optical properties of the substrates forming the object by calculating the refractive index and the absorption coefficient of its constituents in the reconstruction frequency band. We demonstrate with our work the utilization of the SA not only for imaging, but also for material characterization. Consequently, we are able to reconstruct 2D high-resolution spectral maps of the real refractive index at different THz frequencies of the imaged object.**

***Index Terms*—Terahertz imaging, terahertz spectroscopy, material characterization, terahertz time-domain system, synthetic aperture, back-projection, 3D image reconstruction.**

I. INTRODUCTION

AT the junction between microwaves and infrared, THz imaging techniques offer numerous opportunities in non-destructive testing in several industrial sectors like building and construction industry and electrical cables industry [1], [2], quality control of pharmaceuticals [3], archeological studies [4], medical and biomedical imaging [5]–[7], etc.

In a typical THz imaging setup, the object under test is mechanically translated in the focus plane of a THz beam either in reflection or transmission configurations [8], [9]. The THz image is assembled pixel by pixel based on the complex spectrum measured at every scanned point by the focused beam, enabling spectroscopic images of the object. This approach is nevertheless limited to portable and mechanically translatable objects [10]. In specific imaging scenarios, it is more favorable to image an object without translating it, such as large, heavy, or fragile objects. In addition to that, the lateral resolution achieved using a typical imaging setup is defined by the spot size of the focused THz beam which depends on the optical alignment of focusing lenses or mirrors.

To overcome the challenges of the classical imaging setup, the SA technique is considered in the THz domain. SA is a well-established imaging technique initially invented for radar systems in the 1950s [11] and it was later on adopted at RF and microwave frequency bands for a variety of applications in the commercial and defense sectors [12], [13], [14] like topographic imaging [15], air traffic control [16], meteorology [17] and underground resource exploration [18]. Imaging using SA consists of reconstructing an image by creating a numerical focusing lens by back-projecting acquired signals measured at different spatial positions from an illuminated area under test[19]. As a result, the spatial resolution of the image is no longer defined by the aperture of each antenna, but it depends on the space/time localization of the mobile antenna, which enables a high spatial resolution with small radiating elements.

The implementation of the SA technique for imaging in the THz range was demonstrated in previous reports using either electronic or optoelectronic-based systems in reflection configuration. A Vector Network Analyzer (VNA) coupled with frequency extenders was used to demonstrate 3D imaging at four different frequency bands (220-330 GHz, 325-500 GHz, 850-1100 GHz, and 1100-1500 GHz). Four different antennas were needed to generate THz waves at the four frequency bands [20], [21]. To tackle the inherently limited frequency of the VNA, the addition of frequency extenders was necessary to up-convert the low frequency signal from the VNA into the desired frequency range, adding to the bulkiness of the VNA based imaging system [21]. The object was mounted on a mobile platform in order to create a SA while its image was reconstructed from back-projected reflected signals. SA implementation with a THz-TDS system was firstly demonstrated using a photoconductive antenna (PCA) as both emitter and detector, in a monostatic configuration, scanned over the object to create a synthetic planar array [22]. Reflected electric fields acquired at different positions were numerically processed to reconstruct a 3D image of the object over a large frequency band from 0.3 to 1.2 THz. This imaging system was further exploited to differentiate several types of materials of an object from the intensity variations on the image at specific resonance frequencies [23]. The interest of SA-TDS was also demonstrated with 2D imaging of metallic objects within a very large bandwidth of 2.5 THz by measuring the reflected signal from the objects in rotation. The PCA emitter and detector were positioned in a reflection configuration with an angle between the two antennas (without collimating or focusing lenses) and the objects were rotated to mimic a synthetic array [22].

It is worth stating that SA-TDS offers a large bandwidth, coherent detection and does not require the optical focalization system associated with the classical imaging approach to have high range and cross-range resolutions. However, none of the SA systems reported so far, have yet paired SA imaging with spectroscopy analysis to extract the optical parameters of the materials forming the object.

In this work, we experimentally demonstrate 3D THz imaging and spectroscopy analysis based on the SA imaging approach implemented on a TDS system, which is performed in a

transmission configuration for the first time. In our system, the synthetic array is realized by moving a PCA along a scanning plane. We present numerically reconstructed 3D images of a complex planar object (made of air, metal, magnesium oxide and quartz) using the back-projection algorithm. The reconstructed complex data is further used to compute the refractive index and the absorption coefficient of the object. Our proposed approach goes beyond the utilization of the SA imaging technique in previous studies. Instead, we leverage the phase and amplitude of the reconstructed data to calculate the real refractive index and absorption coefficient, pushing SA from being just an imaging tool to a valuable approach for material characterization. This approach is particularly useful for spectroscopy in fields where immobile objects are more common and the elimination of the focusing lenses is favorized. The results show the potential of the proposed approach as an experimental technique for sub-millimeter 3D imaging and spectroscopy in the THz range of multi-material objects. Moreover, our approach has the potential to extend THz imaging beyond traditional reflection-based imaging by favoring substrates with high transmittivity, in contrast to SA in reflection configuration, which requires a big portion of the THz beam to be reflected back to the detector. By exploiting the low dynamic range of the signal in the chosen transmission configuration, we were able to reconstruct 3D images, similar to those demonstrated in reflection configuration, opening doors to test other types of objects.

II. SA-BASED 3D IMAGING AND SPECTROSCOPY

In this section, we briefly recall the numerical process allowing the reconstruction of a 3D image from measured data using a SA. To synthesize a radiating aperture, a mobile antenna is periodically translated on a distance D, with a step d in a two-dimensional plane perpendicular to the direction of propagation (figure 1). For each transmit antenna position $(x_n, y_n = 0, z_n)$, with $n \in [1, N]$ and N the total number of spatial scanned points in the XOZ plan, a temporal signal $s_{mes}(t, x_n, z_n)$ is measured on the stationary receiving antenna.

The 3D image is reconstructed in the frequency domain using an image reconstruction method known as the back projection (BP) algorithm [23]. The BP algorithm acts as a digital lens by compensating the phase of the signals propagated from the antennas to the scene to be imaged. The frequency-dependent reconstructed complex transmittivity of each voxel is expressed as:

$$\tilde{T}_{re}(f_m, x_p, y_p, z_p) \approx \sum_{n=1}^{N} S_{mes}(f_m, x_n, z_n) \cdot e^{-j\frac{2\pi}{c} f_m r_n^p} \quad (1)$$

With c is the speed of the THz wave in vacuum, $m \in [1, M]$ with M the total number of frequency points, and $p \in [1, P]$ with P the total number of voxels of the reconstructed image. $S_{mes}(f_m, x_n, z_n)$ is the Fourier Transform of the measured time domain signal with f_m the frequency. The parameter $r_n^p = \sqrt{(x_p - x_n)^2 + (y_p)^2 + (z_p - z_n)^2}$ is the distance between an antenna n of the planar synthetic array, to a voxel p of the reconstructed 3D matrix.

The intensity of each voxel of the reconstructed 3D image can be expressed as:

$$I(x_p, y_p, z_p) = \left| \sum_{m=1}^{M} \tilde{T}_{re}(f_m, x_p, y_p, z_p) \right| \quad (2)$$

The spatial theoretical resolutions of the resulting 3D image, using a planar synthetic array of isotropic antennas, are expressed as [11]:

$$\Delta_x = \frac{\lambda.R}{D_x}, \ \Delta_y = \frac{c}{BW}, \ \Delta_z = \frac{\lambda.R}{D_z} \quad (3)$$

Where Δx, Δy and Δz are the cross-range, range and elevation resolutions respectively, D_x is the length of the SA along (OX) axis, D_z is the length of the SA along (OZ) axis, BW is the available frequency bandwidth and λ is the wavelength of the propagating beam. However, in reality, the resolution is limited by the divergence of the antenna's radiation pattern [11].

The SA allows a lateral field of view (FOV) of:

$$FOV_x = \frac{\lambda.R}{d_x}, \ FOV_z = \frac{\lambda.R}{d_z} \quad (4)$$

Where d_x and d_z are periodical antenna increments in the synthetic array along X-axis and Z-axis respectively.

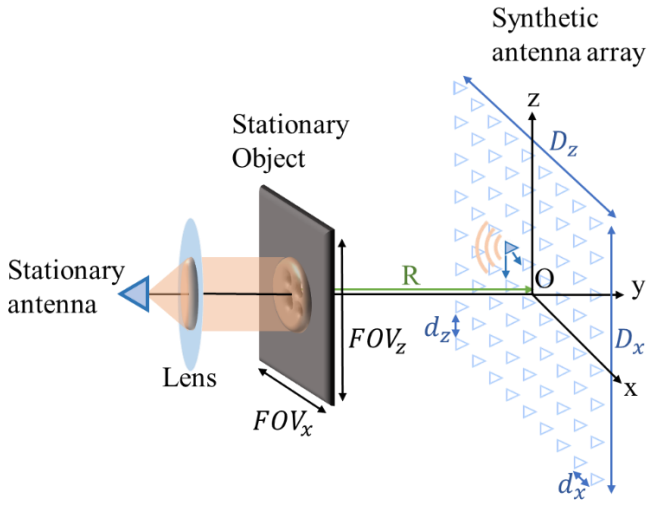

Fig. 1. *Schematic of SA imaging in a transmission configuration. The moving divergent antenna is mechanically scanning the plane XOZ to create a planar synthetic antenna array. At each position of the mobile antenna, the emitted beam passing through the stationary object is focused on the fixed, detecting antenna.*

The complex reconstructed data can be further used to extract the frequency-dependent refractive index $n(f)$ and the absorption coefficient $\alpha(f)$. Similar to classical THz-TDS measurement, our approach requires the measurement of both reference and sample signals. In our study, the reference data was obtained using a synthetic antenna array, similar to the one used for measuring the sample data. The reference measurement is obtained by scanning the emitter antenna step by step while detecting the THz radiation through air (without the object to be imaged) using the stationary detector and a collimating lens. Following the acquisition of the reference data, we reconstructed a reference complex transmittivity

$\tilde{T}_{re_{reference}}(f, x_p, z_p)$ independently from the sample data by applying Equation 1. This allowed obtaining a frequency-dependent reconstructed spectrum at each pixel, which served as a reference spectrum for each corresponding pixel in the sample complex transmittivity $\tilde{T}_{re_{object}}(f, x_p, z_p)$.

Based on the reference and sample reconstructed transmittivities, a complex transmission coefficient of the object is calculated at each frequency f following this equation:

$$\frac{\tilde{T}_{re_{sample}}(f,x_p,z_p)}{\tilde{T}_{re_{reference}}(f,x_p,z_p)} = \rho_{re}(f, x_p, z_p)e^{-j\varphi_{re}(f,x_p,z_p)} \quad (5)$$

This ratio leads to $\rho_{re}(f, x_p, z_p)$ and $\varphi_{re}(f, x_p, z_p)$, the amplitude ratio and phase difference, respectively, between the spectral components of the sample and the reference reconstructed transmittivities.

Consequently, the values of the real part of the refractive index $n(f, x_p, z_p)$, its imaginary part $\kappa(f, x_p, z_p)$ and the absorption coefficient $\alpha(f, x_p, z_p)$ of the object under test can be derived for every pixel of the reconstructed object image using the following equations [24]:

$$n(f, x_p, z_p) = 1 + c\frac{\varphi_{re}(f,x_p,z_p)}{2\pi f e} \quad (6)$$

$$\kappa(f, x_p, z_p) = -\frac{c}{4\pi f e}\ln\left(\tau(f, x_p, z_p)\rho_{re}(f, x_p, z_p)\right) \quad (7)$$

With $$\tau(f, x_p, z_p) = 1 - \frac{(n(f,x_p,z_p)-1)^2}{(n(f,x_p,z_p)+1)^2} \quad (8)$$

$$\alpha(f, x_p, z_p) = \frac{4\pi f}{c}\kappa(f, x_p, z_p) \quad (9)$$

With e the thickness of the sample measured with a digital micrometer gauge (having a precision of +/- 1 micrometer) before performing the THz imaging and spectroscopy experiments. The measured thickness is then used as an input parameter to calculate the parameters above from the reconstructed data.

III. Experimental setup: SA implementation in a THz-TDS

SA-TDS approach was implemented in broadband THz-TDS system (TERA K15 all fiber-coupled Terahertz Spectrometer from Menlo Systems GmbH). The system illustrated in figure 2 is using a femtosecond laser operating at $\lambda = 1550\ nm$. The laser beam is split into a probe and pump beam. The pump beam irradiates a biased photoconductive antenna (PCA) which will emit a THz pulse, while the probe beam is irradiating a second PCA which will generate an electrical signal proportional to the incident THz wave amplitude. The temporal THz pulse allows to acquire a complex spectrum from 0.1 THz to 6 THz. The emitter and receiver PCAs are commercial fiber-coupled TERA15-FC antenna modules in strip line and dipole configurations respectively, paired with a high refractive index silicon (HR-Si) hyper-hemispherical lens at the output side, resulting in a divergence angle of THz radiation of about 14.5°.

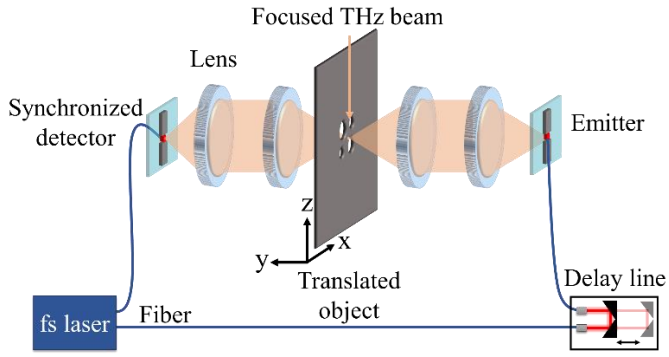

Fig. 2. *Classical focused configuration of THz TDS. The imaged object is mechanically translated in the XOZ plane using a two-axis translation stage. The focal plane of the focused THz beam is achieved using four TPX lenses.*

SA-TDS system was achieved by attaching the emitter antenna to a mechanical 2D translation arm to record the transmitted THz pulse at different spatial positions (figure 3). Both receiver and emitter antennas can be translated to create a synthetic antenna array as they are both lightweight, compact and fiber optic pigtailed PCAs. For simplicity, the emitter antenna was chosen because it is not attached to a current amplifier as in the case of the receiver, which otherwise restrains the range of movement and calls for a more complicated support system to securely move the amplifier together with the receiver.

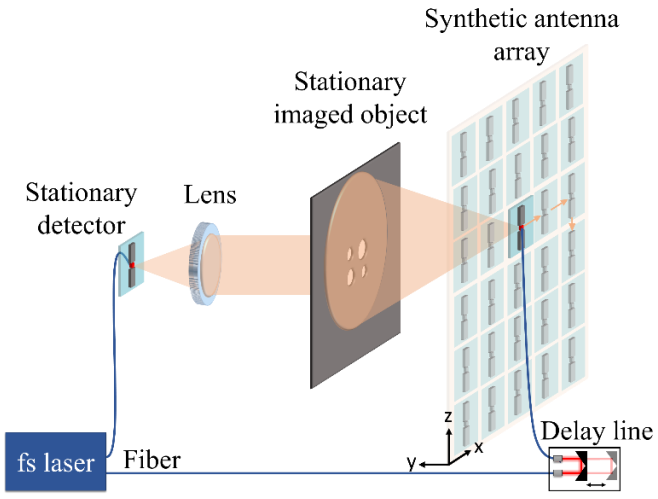

Fig. 3. *Transmission based SA configuration using a THz-TDS for 3D imaging and spectroscopy. A PTFE lens is used to focus the beam onto the fixed detector.*

The merging of the SA approach into the available THz-TDS system allows to dispose of the optical focusing system illustrated in figure 2. However, the elimination of all TPX focusing lenses results in a sensitivity decrease in the system therefore a decline in the dynamic range (DR) of the measured THz pulse. In a four lenses configuration, the DR is 87 dB at 1 THz (figure 4, blue curve) and in lens-free configuration, the

DR falls to 36 dB at 1 THz (figure 4, yellow curve) that is associated with a reduction of the available BW from 6 THz to 3 THz.

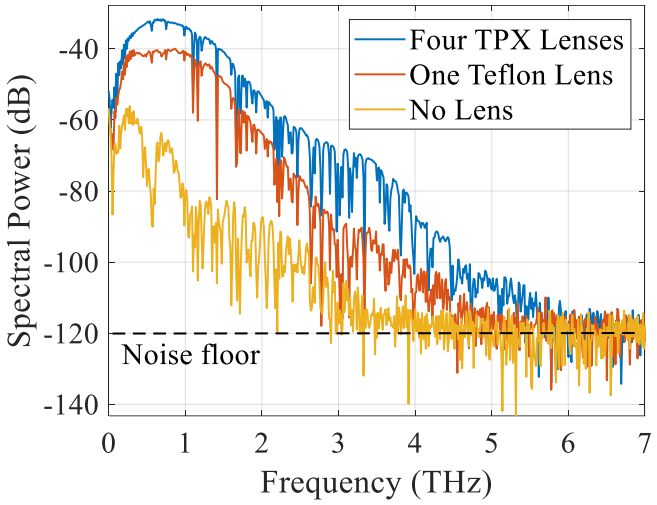

Fig. 4. *Amplitude of spectral power recorded with the full optical system as in a classical focused TDS system (blue curve), with one lens (orange curve) and without any focusing lenses (yellow curve).*

In order to increase the DR without focusing the THz beam, a PTFE plano-convex lens was added in front of the fixed detector (figure 3). The addition of the lens does not affect the topology of the synthetic antenna array or the image reconstruction algorithm but improves the DR of the signal to 80 dB at 1 THz (figure 4, orange curve).

IV. Measurement Results and Discussions

To demonstrate SA-TDS imaging in transmission configuration with the TDS system, we choose a thin metallic plate ($2 \times 2\ cm^2$) with four open circular holes with different diameters from 3 mm to 6 mm (figure 5). A sample of MgO (e = 530 µm) is placed behind the hole of 6 mm diameter and another sample of quartz (e = 530 µm) is placed behind the hole of 5 mm diameter. These samples with different refractive indexes will be evaluated for their dielectric THz properties along with the 3D reconstruction of the overall object.

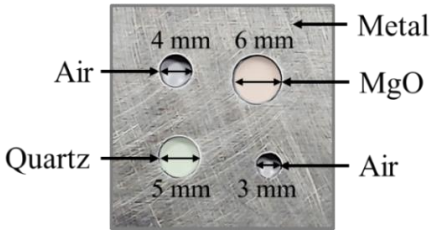

Fig. 5. *Object under test: a metallic plate of 2x2 cm² with four holes, two holes with diameters 6 mm and 5 mm containing MgO (false-colored in orange) and quartz (false-colored in green) respectively. The other smaller holes of 3 and 4 mm contain air. The thickness of the two substrates is 530 µm.*

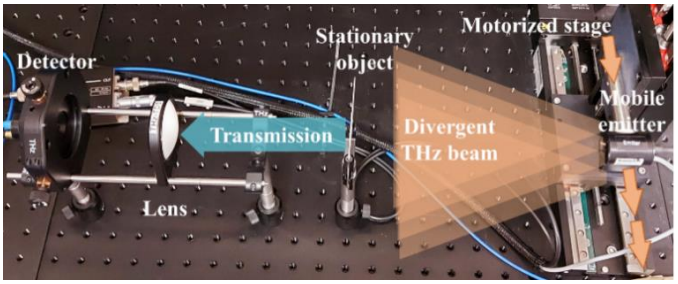

Fig. 6. *Top view picture of the 3D SA-THz imaging system taken from top view, including a sketch of the divergent THz beam and propagation direction.*

The image reconstruction was performed from 0.6 THz to 1 THz since this frequency band provides a good tradeoff between DR, atmospheric absorption of the THz beam, and a smaller wavelength for a higher image resolution. To further improve the DR, each signal is generated from 78 averaged THz time-domain traces.

All measurements are performed under typical indoor atmospheric conditions at room temperature of 23°C. The rest of the parameters of the synthetic array and the acquisition process are resumed in table 1.

TABLE I
PARAMETERS OF THE SYNTHETIC ARRAY

Symbol	Parameter	Value
$\boldsymbol{BW}$	Bandwidth	0.6 THz to 1 THz
$\boldsymbol{D_x = D_z}$	SA length along x-axis and z-axis	10 cm
$\boldsymbol{d_x = d_z}$	Step size along x-axis and z-axis	2 mm
$\boldsymbol{R}$	Object range	21 cm
$\Delta_x = \Delta_z$	X and Z cross-range resolutions	671 µm* @ 1 THz
Δ_y	Range resolution	750 µm
$\boldsymbol{FOV_x = FOV_z}$	Field of View along x-axis and z-axis	3 cm @ 1 THz
$\boldsymbol{avg}$	Number of averaged signals acquired at each position	78

**Taking into account the divergence of the antenna*

The cross-range resolution is 671 µm at FWHM at 1 THz using the antenna with a divergent beam of 14.5° and the array parameters indicated in table 1, estimated through a calculation of the point spread function (PSF) of the imaging system. The

estimated experimental resolution is very close to the theoretical resolution of 600 µm.

The intensity of the reconstructed 3D image using the BP algorithm of the object under test is shown in figure 7. The shapes of the four holes are correctly reproduced as well as their spatial positions on the metallic plate. The reconstructed image is located at a depth position of y=21 cm, which corresponds to distance between the object and the synthetic array.

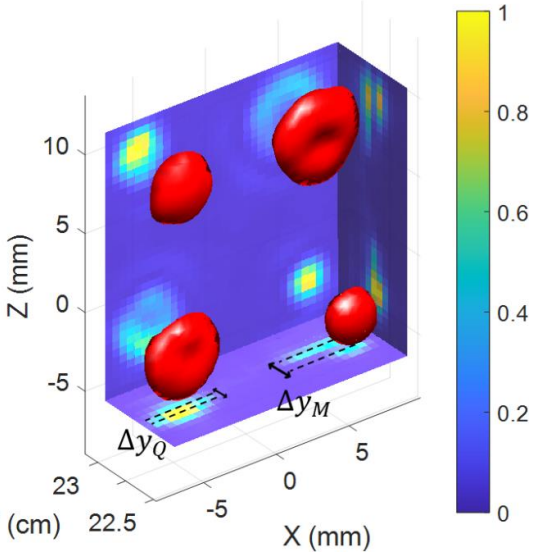

Fig. 7. *3D image and associate projections on XOY, XOZ, and YOZ planes, reconstructed between 0.6 THz and 1 THz with sub-millimeter range and cross-range resolutions.*

This result underlines the strength of the imaging technique that does not require any input information about the shape or the size of the sample. Amplitude variations between the four holes are apparent when projecting the reconstructed amplitude image on the XOZ plane as each projection displays a different level of intensity proportional to the refractive index of mediums in the holes. By projecting the 3D reconstructed image on the XOY and YOZ planes (figure 7), the distance between the different reconstructed zones can be used to retrieve the value of the group refractive index of the medium using the equation:

$$n_g = 1 + \frac{\Delta y}{e} \tag{10}$$

where Δy is the distance between the projection of the reconstructed image of a dielectric material (behind an air hole) and the reconstructed image of an air hole (reference), and e is the thickness of the sample.

Thus, for a distance between the reconstructed quartz area and air of $\Delta y_Q = 500\ \mu m$, the group refractive index is $n_{g_{quartz}} = 1.94$ while for MgO ($\Delta y_M = 1000\ \mu m$), $n_{g_{MgO}} = 2.88$. The projections on XOY and YOZ planes coming from the areas of MgO, and the air are clearly separated on figure 7 since the spatial depth between the two reconstructed zones is higher than the depth resolution of 750 µm of our synthetic array while the separation corresponding to the projections of quartz and air is less visible ($\Delta y_Q < 750\ \mu m$).

We should note that the SA trajectories deviations, caused by the error of the positioning of the antenna during data acquisition, are limited to 5 µm in both directions according to the supplier of the translation motor used in our experimental setup. This positioning error results in a phase modulation of approximately $|\Delta\varphi| \leq \frac{\pi}{50} \ll \frac{\pi}{8}$, so in this case the impact of phase error on the SA can be neglected. [25].

To further demonstrate the capabilities of the proposed approach for material characterization, the reconstructed data is used to extract the refractive index and absorption coefficient as indicated in the previous section.

The reference time domain signal through air and through the quartz and MgO samples after the reconstruction of the image are presented in figure 8.

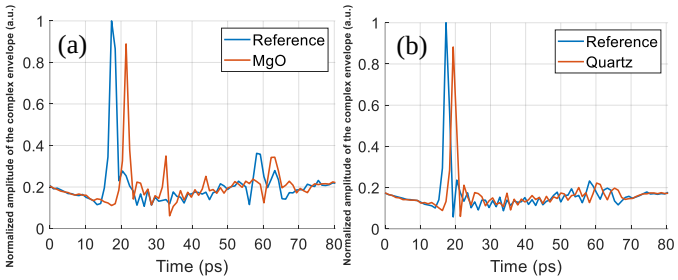

Fig. 8. *Reconstructed temporal signals at two different coordinates: (a) MgO at x=6mm and z=5mm (orange curve) and the reference temporal signal corresponding to the same reconstructed coordinates (blue curve). (b) Quartz at x=-3mm and z=-3mm (orange curve) and the corresponding reference reconstructed temporal signal (blue curve).*

The selected materials are non-dispersive, and their thickness is 500 µm for each, which is thick enough for the propagated short pulse to create an isolated echo pulse from the main signal. The transmitted temporal signal through the quartz does not display any visible multiples (figure 8.a.), while MgO exhibits one reflection peak after a trip in the substrate since it has a higher refractive index than quartz (figure 8.b.). In this particular case, the echo on the temporal signal can be removed using simple windowing techniques in the same way echoes could be removed when using a classical THz-TDS set up for material characterization.

Based on the reference and sample reconstructed transmittivities, a complex transmission coefficient of the object is calculated at each frequency following the equation 5. After computing $n(f, x_p, z_p)$ using equation 6, the frequency dependent refractive index, taken at the center pixel of the holes containing MgO and quartz, are presented in figure 9.a from 0.6 THz to 1 THz. The average refractive index on the investigated frequency band of MgO is $n_{M_{avg}} = 3.01$ and the average refractive index of quartz is $n_{Q_{avg}} = 2.07$, values which are consistent with previous reports [26],[27].

The absorption coefficient of each pixel of the reconstructed image of the object is calculated using equation (7). In figure 9.b, the absorption coefficient of the center pixel of the hole containing MgO (blue curve) and the center pixel of the hole containing quartz (orange curve) are presented from 0.6 THz to

1 THz. The absorption coefficient of MgO is extremely low, less than 3 cm^{-1} in magnitude, the material being nearly transparent between 0.6 THz and 1 THz [26]. The quartz sample also presents a very low absorption coefficient of less than 1.5 cm^{-1} between 0.6 THz and 1 THz [27].

From the computed $n(f, x_p, z_p)$, 2D maps of the refractive index of the object could be reconstructed at each frequency of the reconstruction frequency band. As shown in figure 10, the index of the areas of the air holes, MgO sample and quartz sample are correctly reconstructed at 603 GHz and 990 GHz, emphasizing the interest of SA-TDS for imaging and material characterization in the THz rang. A higher resolution could be attained by placing the system in a dry air chamber to access higher frequencies of the THz spectrum generated by the TDS.

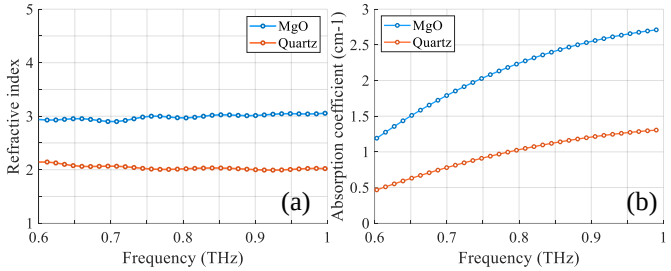

Fig. 9. ***(a)*** *Frequency dependent refractive index computed from reconstructed data using equation (6) at two different coordinates: MgO at x=6mm and z=5mm (blue curve) and quartz at x=-3mm and z=-3mm (orange curve).* ***(b)*** *Frequency dependent absorption coefficient computed from reconstructed data using equation (9) at two different coordinates: MgO at x=6mm and z=5mm (blue curve) and quartz at x=-3mm and z=-3mm (orange curve). The reference measurement for the absorption coefficient is obtained using the metallic object without the dielectric substrates.*

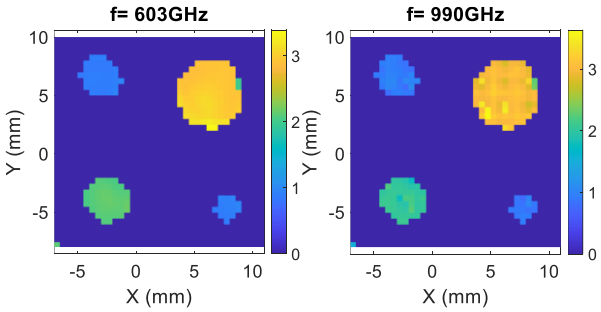

Fig. 10. *2D maps of the reconstructed refractive index of the dielectric samples within the imaged object at two different frequencies (a) at 603 GHz and (b) at 990 GHz. The 3D imaging performed beforehand is used to define the areas of interest, in which the refractive index reconstruction could be performed. The area of the metallic plate is set with a null refractive index for the visual aspect.*

V. CONCLUSION

We presented an approach to broadband 3D imaging and spectroscopy in the THz domain. The measurement setup combines the non-focused radiation from a THz-TDS system and the SA imaging technique implemented in the transmission configuration. The experimental results show that the technique can generate 3D images with sub-millimeter resolution in a frequency band up to 1 THz of a stationary planar object integrating different materials. The 3D amplitude image can be used to compute the group refractive index of different constituents of the sample, providing a first information on the different integrated materials. We further demonstrate the pairing of SA technique and spectroscopy analysis of the object under test, by using the reconstructed amplitude and phase to obtain the refractive index and the absorption coefficient, which enables 2D spectroscopy mapping for each frequency of the investigated reconstruction band.

This firstly reported approach, combining imaging and spectroscopy for material characterization based on SA TDS THz in transmission configuration, can be highly relevant for non-destructive testing and spectral characterization of fixed objects with different permittivity. This method, which is extremely appropriate for the characterization of low absorption materials, could be easily implemented in reflection configuration, which is more adapted for the characterization of absorptive or opaque materials in the THz range.

The particular implementation we proposed opens robust perspectives for real-time 3D imaging and spectroscopy, by replacing the mechanical scanning of the antenna used to create a SA with a real antenna array illuminating the scene instantly.

REFERENCES

[1] Y. H. Tao, A. J. Fitzgerald, and V. P. Wallace, “Non-Contact, Non-Destructive Testing in Various Industrial Sectors with Terahertz Technology,” *Sensors*, vol. 20, no. 3, p. 712, Jan. 2020, doi: 10.3390/s20030712.

[2] D. Nüßler and J. Jonuscheit, “Terahertz based non-destructive testing (NDT): Making the invisible visible,” *Tm - Tech. Mess.*, vol. 88, no. 4, pp. 199–210, Apr. 2021, doi: 10.1515/teme-2019-0100.

[3] M. R. Patil, S. B. Ganorkar, A. S. Patil, and A. A. Shirkhedkar, “Terahertz Spectroscopy: Encoding the Discovery, Instrumentation, and Applications toward Pharmaceutical Prospectives,” *Crit. Rev. Anal. Chem.*, vol. 52, no. 2, pp. 343–355, Feb. 2022, doi: 10.1080/10408347.2020.1802219.

[4] M. Mikerov, R. Shrestha, P. van Dommelen, D. M. Mittleman, and M. Koch, “Analysis of ancient ceramics using terahertz imaging and photogrammetry,” *Opt. Express*, vol. 28, no. 15, p. 22255, Jul. 2020, doi: 10.1364/OE.399336.

[5] M. Supriya and A. V. Samuel, “Terahertz technology: A Review on dental perspective,” *J Pharm Sci*, vol. 12, p. 6, 2020.

[6] A. I. Nikitkina *et al.*, “Terahertz radiation and the skin: a review,” *J. Biomed. Opt.*, vol. 26, no. 04, Feb. 2021, doi: 10.1117/1.JBO.26.4.043005.

[7] A. D’Arco, M. D. Di Fabrizio, V. Dolci, M. Petrarca, and S. Lupi, “THz Pulsed Imaging in Biomedical Applications,” *Condens. Matter*, vol. 5, no. 2, p. 25, Apr. 2020, doi: 10.3390/condmat5020025.

[8] B. B. Hu and M. C. Nuss, “Imaging with terahertz waves,” *Opt. Lett.*, vol. 20, no. 16, p. 1716, Aug. 1995, doi: 10.1364/OL.20.001716.

[9] I. Malhotra and G. Singh, *Terahertz Antenna Technology for Imaging and Sensing Applications*. Cham: Springer International Publishing, 2021. doi: 10.1007/978-3-030-68960-5.

[10] X.-C. Zhang and J. Xu, *Introduction to THz Wave Photonics*. Boston, MA: Springer US, 2010. doi: 10.1007/978-1-4419-0978-7.

[11] M. Soumekh, *Synthetic Aperture Radar Signal Processing*, vol. 7. New York : Wiley, 1999.

[12] T. Obata, M. Arai, S. Asada, T. Imaizumi, H. Saito, and S. Shirasaka, “The Latest Status of Our Commercial Small Synthetic Aperture Radar Satellite Constellation,” in *IGARSS 2020 - 2020 IEEE International Geoscience and Remote Sensing Symposium*, Waikoloa, HI, USA: IEEE, Sep. 2020, pp. 3578–3580. doi: 10.1109/IGARSS39084.2020.9323284.

[13] G.-C. Sun, Y. Liu, J. Xiang, W. Liu, M. Xing, and J. Chen, "Spaceborne Synthetic Aperture Radar Imaging Algorithms: An overview," *IEEE Geosci. Remote Sens. Mag.*, vol. 10, no. 1, pp. 161–184, Mar. 2022, doi: 10.1109/MGRS.2021.3097894.

[14] B. Ding, G. Wen, C. Ma, and X. Yang, "Target recognition in synthetic aperture radar images using binary morphological operations," *J. Appl. Remote Sens.*, vol. 10, no. 4, p. 046006, Oct. 2016, doi: 10.1117/1.JRS.10.046006.

[15] R. Bürgmann, P. A. Rosen, and E. J. Fielding, "Synthetic Aperture Radar Interferometry to Measure Earth's Surface Topography and Its Deformation," *Annu. Rev. Earth Planet. Sci.*, vol. 28, no. 1, pp. 169–209, May 2000, doi: 10.1146/annurev.earth.28.1.169.

[16] A. Reigber *et al.*, "Very-High-Resolution Airborne Synthetic Aperture Radar Imaging: Signal Processing and Applications," *Proc. IEEE*, vol. 101, no. 3, pp. 759–783, Mar. 2013, doi: 10.1109/JPROC.2012.2220511.

[17] B. Puysségur, R. Michel, and J.-P. Avouac, "Tropospheric phase delay in interferometric synthetic aperture radar estimated from meteorological model and multispectral imagery," *J. Geophys. Res.*, vol. 112, no. B5, p. B05419, May 2007, doi: 10.1029/2006JB004352.

[18] V. K. Dang, T. D. Nguyen, N. H. Dao, T. L. Duong, X. V. Dinh, and C. Weber, "Land subsidence induced by underground coal mining at Quang Ninh, Vietnam: persistent scatterer interferometric synthetic aperture radar observation using Sentinel-1 data," *Int. J. Remote Sens.*, vol. 42, no. 9, pp. 3563–3582, May 2021, doi: 10.1080/01431161.2021.1875513.

[19] T. Ager, "An Introduction to Synthetic Aperture Radar Imaging," *Oceanography*, vol. 26, no. 2, Jun. 2013, doi: 10.5670/oceanog.2013.28.

[20] A. Batra *et al.*, "Short-Range SAR Imaging From GHz to THz Waves," *IEEE J. Microw.*, vol. 1, no. 2, pp. 574–585, Apr. 2021, doi: 10.1109/JMW.2021.3063343.

[21] A. Batra, M. Wiemeler, D. Gohringer, and T. Kaiser, "Sub-mm Resolution 3D SAR Imaging at 1.5 THz," in *2021 Fourth International Workshop on Mobile Terahertz Systems (IWMTS)*, Essen, Germany: IEEE, Jul. 2021, pp. 1–5. doi: 10.1109/IWMTS51331.2021.9486780.

[22] D. Damyanov *et al.*, "High Resolution Lensless Terahertz Imaging and Ranging," *IEEE Access*, vol. 7, pp. 147704–147712, 2019, doi: 10.1109/ACCESS.2019.2934582.

[23] A. W. Doerry and J. M. Edward E., "Basics of Backprojection Algorithm for Processing Synthetic Aperture Radar Images," p. 58, 2016.

[24] M. Naftaly and R. E. Miles, "Terahertz time-domain spectroscopy of silicate glasses and the relationship to material properties," *J. Appl. Phys.*, vol. 102, no. 4, p. 043517, Aug. 2007, doi: 10.1063/1.2771049.

[25] A. Batra, M. El-Absi, M. Wiemeler, D. Gohringer, and T. Kaiser, "Indoor THz SAR Trajectory Deviations Effects and Compensation With Passive Sub-mm Localization System," *IEEE Access*, vol. 8, pp. 177519–177533, 2020, doi: 10.1109/ACCESS.2020.3026884.

[26] J. Han, B. K. Woo, W. Chen, M. Sang, X. Lu, and W. Zhang, "Terahertz Dielectric Properties of MgO Nanocrystals," *J. Phys. Chem. C*, vol. 112, no. 45, pp. 17512–17516, Nov. 2008, doi: 10.1021/jp805880p.

[27] M. Naftaly and R. E. Miles, "Terahertz Time-Domain Spectroscopy for Material Characterization," *Proc. IEEE*, vol. 95, no. 8, pp. 1658–1665, Aug. 2007, doi: 10.1109/JPROC.2007.898835.